



Contents lists available at SciVerse ScienceDirect

# International Journal of Rock Mechanics & Mining Sciences

journal homepage: [www.elsevier.com/locate/ijrmms](http://www.elsevier.com/locate/ijrmms)

## Strength evolution in heterogeneous granular aggregates during chemo–mechanical compaction

Baisheng Zheng\*, Derek Elsworth

Energy and Mineral Engineering, Energy Institute and G<sup>3</sup> Center, Penn State University, University Park, PA, USA

### ARTICLE INFO

#### Article history:

Received 3 February 2012

Received in revised form

24 December 2012

Accepted 27 December 2012

#### Keywords:

Strength

Pressure solution

Granular mechanics

Micro scale simulation

### ABSTRACT

We present a model capable of following the evolution of strength in granular aggregates where dissolution driven by local contact stresses may result in grain interpenetration, precipitation and bonding. At each particle–particle contact mineral redistribution results from the serial processes of stress-enhanced dissolution, mass diffusion along the fluid film separating grain boundaries and then mass ejection into the pore space — where it may then be reprecipitated on the pore wall. All of these processes contribute to strength gain during chemical compaction by two principal mechanisms. First, stressed particles merge together by dissolution to reduce the pore space, remove existing microfractures and increase the contact area. Second, mass is transported by diffusion into the pore space where overplating increases particle size and initiates neck growth between particles and increases the cross-sectional contact between particles. We complete numerical experiments on unconfined prismatic samples to evaluate the influence of time dependent strengthening on initially unbonded sands undergoing diagenesis then failure. Strength gain is evaluated both by proxy from scaling with the growth of contact area and neck strength and by numerically failing the sample at different stages of compaction. The proxy method overestimates ultimate strength by less than ~10%. For particle of original radius ~200 μm grow by precipitation by ~2% and with a neck thickness of 20 μm as a result of chemo–mechanical compaction. This results in an increase in cohesion from 0 MPa to ~22 MPa. Feedbacks of pressure solution on the mechanical response results both in a reduction in local particle–particle contact stresses and a more uniform distribution of stresses in the aggregate. Strength evolution is evaluated by two proxies and by numerical experimentation to failure that shows an ~50% increase of peak stress of the granular system after chemo–mechanical compaction compared with that before chemo–mechanical compaction.

© 2013 Elsevier Ltd. All rights reserved.

### 1. Introduction

Sediments and fault gouges represented as granular aggregates may lithify by diagenetic transformations with impact on the material properties of strength, stiffness and permeability. Significant strength recovery or augmentation is observed between earthquakes [1] and in experimental measurements [2,3] with this time dependent fault strengthening well explained by empirical rate-state friction laws [4,5]. However, the processes contributing to this behavior remain ill constrained. The interaction of mechanical and chemical effects clearly exerts significant influence on the evolution of strength [6] and permeability [7] of granular aggregates and of fractures [8]. These feedbacks may involve removing porosity by stress-mediated dissolution [8,9], augmenting porosity by dissolution and wormholing [10–12] or the occluding of porosity by precipitation [13–15].

Similarly, changes in strength result from interface bonding mediated by dissolution and precipitation [6,16], by rearrangement of the particles, [17] and by sub-critical crack growth among other mechanisms [18]. These processes that evolve at the microscopic scale exert important influences on the macroscopic behavior of granular media and are important in understanding rupture, reactivation and healing on faults and in linking triggered-seismicity and permeability–evolution in geothermal, sequestration and hydrocarbon reservoirs. This work focuses on the effects of stress-mediated chemical effects in defining the evolution of strength during chemical compaction.

Chemical compaction result where the elevated contact stresses at grain–grain or asperity–asperity contacts elevates the chemical potential of the mineral allowing the presence of a water film [19,20] to redistribute the dissolving mass. This in turn allows the particles move closer together, to reduce the pore space and to increase the density of the system. Dissolution at the stressed contacts is thermodynamically favored [21]. The concentration of the dissolved mineral matter in the contact area is elevated over that

\* Corresponding author.

E-mail address: [bshzheng@gmail.com](mailto:bshzheng@gmail.com) (B. Zheng).

in the pore space allowing diffusion from the high concentration intergranular area to the low concentration pore space. Eventually, with the changing of mass concentration, mineral reprecipitation to the hydrostatically stressed pore walls may occur, depending on the rates of flushing of the pore space with any advective flux. In this case the growth of a neck between two particles may join two initially contacting particles together with a cohesive bond. This will result in the growth of individual particles into collections of bonded particles that are larger and more irregular (not spherical) with implications on strength and dilational behavior. Due to compaction of the granular assemblage, the filling of the pore space, redistribution of mass, an increase in the contact and cross-sectional areas, the evolution of strength may be significantly affected [6,22,23] as observed in crustal rocks.

A variety of models have been applied to represent the mechanics of chemical compaction [7,19,24–29]. These include lumped-parameter approaches [6] for the compaction of a single grain–grain assemblage and by inference relate this to reservoir diagenesis. This model is applied [6] to explain fault zone restrengthening and frictional healing by evaluation of changes in contact area induced by pressure solution. Other approaches focus on explaining observed response by rate-state friction laws [30,31] which describe behavior at the macroscopic scale. A similar model proposed by Revil in 2006 [29] which is modified from Revil in 1999 [9] used a Cole–Cole distribution of relaxation times and nonlinear compactional law at high effective stresses. In this work we examine the effect of heterogeneous mixtures of particles to determine the influence of grain size distribution on rates of strength gain using a model that accommodates the arrest of compaction by oversaturated fluids [32] and therefore accommodates the role of fluid fluxes in the diagenesis of reservoirs and faults. A fully coupled granular mechanics model is developed to accommodate heterogeneous distributions of particles where the evolution of strength may be followed during mechanical and chemical compaction.

## 2. Background

Strength evolution in heterogeneous granular material occurs during chemical compaction where stress-mediated redistribution of mineral matter occurs at each stressed contact resting within a saturated solution. The redistribution of mineral mass follows three serial processes of (i) dissolution at the stressed contact, (ii) diffusion along the contact controlled by the gradient in concentration, and then (iii) reprecipitation on the less-stressed wall of the pore.

### 2.1. Chemical model

Mechanically-mediated chemical compaction occurs as contact stresses elevate the chemical potential of the solid in the presence of water. This elevated potential favors dissolution into the water film, diffusion along the grain contact and potentially reprecipitation as the mineral mass is ejected into the pore fluid. This behavior may be represented (Fig. 1) by the three processes of (i) dissolution at the stressed interfaces of grain-to-grain contacts (Fig. 1(c,d)), (ii) diffusive transport of dissolved matter from the interface to the pore space, and finally (Fig. 1(c,d)), (iii) reprecipitation at the wall of the pore space [19,33] (Fig. 1(c–e)). The process is driven by differences in effective normal stress, hence the normal component of solid chemical potential  $\Delta\mu$ , between grain contacts and free pore walls [21,26,34] is defined as

$$\Delta\mu = \sigma_a V_m + \Delta f - U_s \quad (1)$$

where  $V_m$  is the molar volume,  $\Delta f$  is the molar Helmholtz free energy and  $U_s$  is the surface energy term;  $\sigma_a$  represents the disjoining pressure, which is the function of the effective stress over the ratio of the contact area to the maximum cross-sectional area.

In defining mass redistribution for the serial processes of dissolution, diffusion, and precipitation, it is convenient to utilize the mineral mass fluxes. See for example the details in Ref. [7].

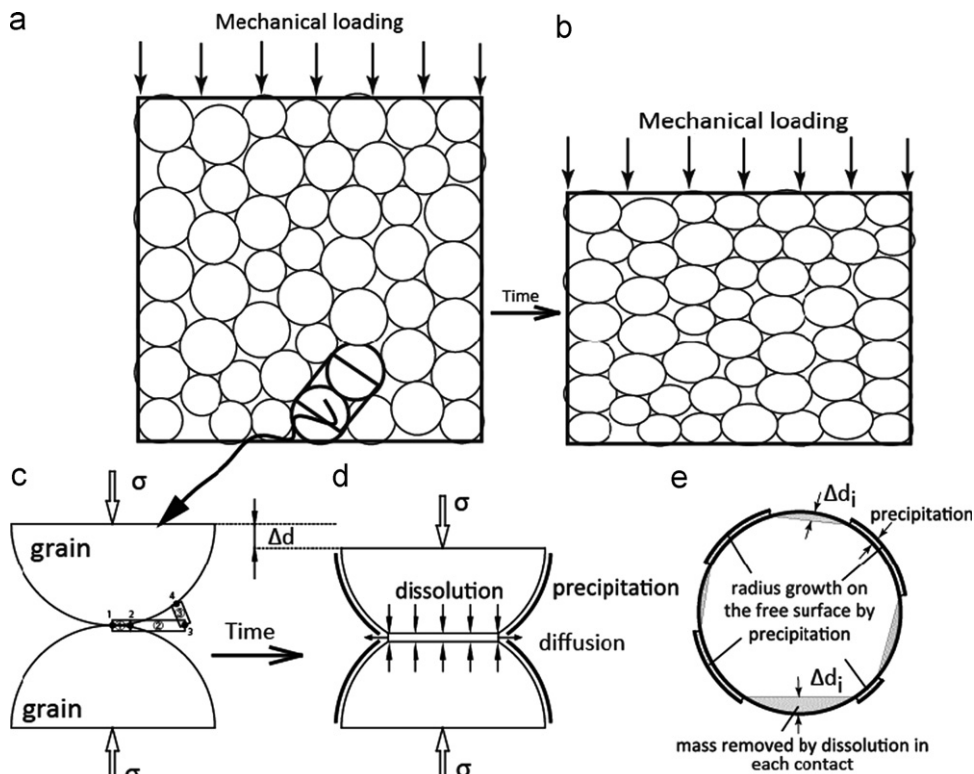


Fig. 1. Schematic illustration of pressure solution for macroscopic aggregate and microscopic twin contacting grains.

With the driving force for pressure solution represented by the chemical potential difference in Eq. (1), dissolution at the grain–grain contacts will first occur which will provide a source of mass transported by the later processes of diffusion and reprecipitation. The dissolution mass flux,  $dM_{diss}/dt$  [9,35], is given by

$$\frac{dM_{diss}}{dt} = k^+ A_i \exp\left(\frac{\Delta\mu}{RT}\right) \left(1 - \frac{\tilde{C}_i}{C_{eq}^\sigma}\right) \quad (2)$$

where  $k^+$  is the forward (dissolution) rate constant and  $A_i$  is the reaction area.  $R$  is the gas constant and  $T$  is current absolute temperature;  $\tilde{C}_i$  is the mean current concentration of aqueous material in the stressed fluid film,  $C_{eq}^\sigma = a_{SiO_2} C_{eq}^h$  is the solubility of aqueous matter in the state of non-hydrostatic stress. Similarly, with the activity of mineral matter in the hydrostatic pore space (subscript by  $p$ ) set to unity [36], the matter precipitated from aqueous to the solid, which facilitates neck growth and the growth in radius of particles can be calculated as

$$\frac{dM_{pre}}{dt} = k^+ A'_p \left(1 - \frac{\tilde{C}_p}{C_{eq}^h}\right) \quad (3)$$

where  $A'_p$  is total available surface area within the pore space, either as a ring around the periphery of the contact-plane between two spheres and accommodating neck growth or on the pore wall. The propensity for dissolution or for precipitation is given by the resulting sign of the bracketed term. In the full iterative scheme, both  $A'_p$  in Eq. (3) and  $A_{ix}^i$  in Eq. (2) evolve in time with the progression of interpenetration.

Dissolution of mass from the solid state to the aqueous state elevates the concentration in the interfacial water film at the contact between two grains. This in turn activates mass transfer by diffusion due to the difference in concentration in the water film between the centers of the contact to the pore periphery. (See Fig. 1(c), from node 1 to 2, then to 3, with precipitation occurring at node 4). The rate of mass transport by molecular diffusion from node 1 to node 2 with time can be deduced from Fick's law as

$$\frac{dM_{dif}}{dt} = \frac{2\pi D_1 \omega}{\tau_f \ln(r_{gc}/r_g)} (\tilde{C}_i - \tilde{C}_n) \quad (4)$$

where we assume that the neck is uniform and exhibits a large diffusive tortuosity. From node 3 to node 4, mass is carried by bulk diffusion at a rate given by

$$\frac{dM_{dif}}{dt} = \frac{8D_b \omega}{\tau_f} (\tilde{C}_n - \tilde{C}_p) \quad (5)$$

where the thickness of the water film is  $\omega = 4$  nm [7,19], the tortuosity correction is  $\tau_f = 10$  [37], and  $D_b$  is the coefficient of bulk diffusion with average concentrations given within the granular interface  $\tilde{C}_i$ , at the grain periphery  $\tilde{C}_n$ , and in the center of the pore space  $\tilde{C}_p$ .

An algorithm that accommodates these three serial mechanisms of dissolution, diffusion then re-precipitation is implemented at individual grain–grain contacts in the granular mechanics model presented here. Two hemispheres represent each grain–grain contact as a single element (see Fig. 1). At the beginning of the calculation the concentration of the mineral in the interface (this is initially a point contact) and the pore are set to be identical. Once stressed, mass transport by the three serial processes of dissolution, diffusion and reprecipitation are calculated simultaneously through Eqs. (2)–(4) and at each time-step,  $\Delta t$ . This is used to capture neck growth concurrent with the other chemical processes and utilizes the three element model with four separate nodal concentrations. For each element, the difference of mass flow in and out results in changes in concentration, so for each element, we have the following equations at each time

step:

$$\dot{C}_i V_i = \frac{dM_{diff}}{dt} - D_i (\tilde{C}_i - \tilde{C}_n) \quad (6)$$

$$\dot{C}_n V_n = \frac{dM_{prec1}}{dt} + D_i (\tilde{C}_i - \tilde{C}_n) - D_b (\tilde{C}_n - \tilde{C}_p) \quad (7)$$

$$\dot{C}_p V_p = \frac{dM_{prec2}}{dt} + D_b (\tilde{C}_n - \tilde{C}_p) \quad (8)$$

where  $V_i$  is total volume within the individual grain–grain contacts,  $V_n$  is pore volume around the contact interface,  $V_p$  is pore volume that excludes  $V_n$ , and  $D_i$  and  $D_b$  are the molecular diffusion and bulk diffusion respectively, The over-dot refers to the time rate of change of the given quantity. The volumes  $V_i$ ,  $V_n$  and  $V_p$ , and the areas derived from them are relative quantities. Combining Eqs. (6)–(8) produces the following linear system (by redistributing source terms):

$$\begin{Bmatrix} k^+ A_{rx}^i a_{SiO_2} \\ k^+ A_{rx}^n \\ k^+ A_{rx}^p \end{Bmatrix} = \begin{bmatrix} V_i & 0 & 0 \\ 0 & V_n & 0 \\ 0 & 0 & V_p \end{bmatrix} \begin{Bmatrix} \dot{C}_i \\ \dot{C}_n \\ \dot{C}_p \end{Bmatrix} + \begin{bmatrix} \left(\frac{k^+ A_{rx}^i}{DC_{eq}^h} + D_i\right) & -D_i & 0 \\ -D_i & \left(\frac{k^+ A_{rx}^n}{DC_{eq}^h} + D_i + D_b\right) & -D_b \\ 0 & -D_b & \left(\frac{k^+ A_{rx}^p}{DC_{eq}^h} + D_b\right) \end{bmatrix} \begin{Bmatrix} C_i \\ C_n \\ C_p \end{Bmatrix} \quad (9)$$

Eq. (9) mimics the general finite element formalism,  $q = S\dot{h} + Kh$ , which admits the implicit solution,  $h_{t+\Delta t} = [K + \frac{1}{\Delta t}S]^{-1} [q + \frac{1}{\Delta t}Sh_t]$ . Performing the multiplication yields,

$$\begin{Bmatrix} C_i \\ C_n \\ C_p \end{Bmatrix}_{t+\Delta t} = \begin{bmatrix} \left(\frac{k^+ A_{rx}^i}{DC_{eq}^h} + D_i\right) & -D_i & 0 \\ -D_i & \left(\frac{k^+ A_{rx}^n}{DC_{eq}^h} + D_i + D_b\right) & -D_b \\ 0 & -D_b & \left(\frac{k^+ A_{rx}^p}{DC_{eq}^h} + D_b\right) \end{bmatrix}_t^{-1} \times \left\{ k^+ A_{rx}^i a_{SiO_2} + \frac{V_i C_i}{\Delta t} k^+ A_{rx}^n + \frac{V_n C_n}{\Delta t} k^+ A_{rx}^p + \frac{V_p C_p}{\Delta t} \right\}_t \quad (10)$$

In the heterogeneous granular system the particle size and the stress state is different from one contact to another. The mass will be redistributed by the concentration gradient induced by dissolution at the particle–particle contacts. For the fluid network (see Fig. 2(a)) a triangular element is used to represent the fluid domain with the connection between the centers of adjacent fluid domains (triangles) forming the fluid transmission network which allows the communication of the mass between different fluid domains as driven by the gradient of concentration.

## 2.2. Mechanical model

The coupling between the mechanical and chemical behaviors is completed through the iterative solution of Newton's second law in a standard fashion within the granular mechanics algorithm (PFC<sup>2D</sup>). An appropriate constitutive model [38,39] must include the non-reactive mechanical behavior supplemented by the behavior induced by chemical compaction. A parallel bond model is chosen to represent the effect of cementation between contacting particles.

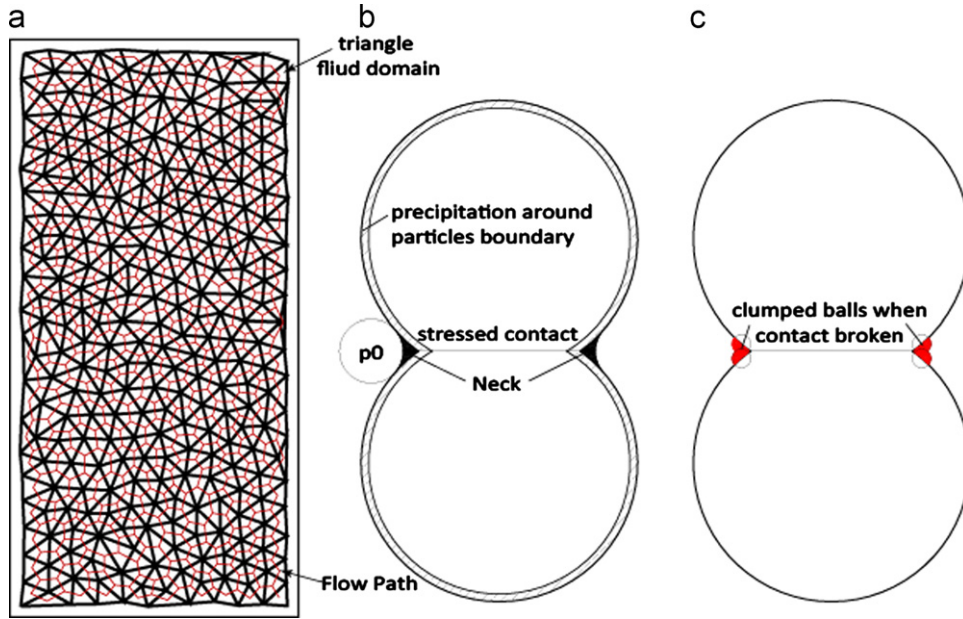


Fig. 2. (a) Fluid network of the granular system; (b) neck growth at each contact; and (c) neck breaks as clumped particles.

2.2.1. Contact model

Before chemo-mechanical loading, the material is unbonded and a Hertzian contact model [39] is used to represent the mechanical behavior of the granular system. The normal force and shear force can be calculated for each contact as

$$\begin{cases} F_i^n = k^n U^n n_i \\ \Delta F_i^s = -k^s \Delta U^s \end{cases} \quad (11)$$

where the normal force  $F_i^n$  is proportional to normal displacement  $U^n$  and scales with the coefficient of normal stiffness  $k^n$ . An increment of shear force  $\Delta F_i^s$  is controlled by an increment of shear displacement  $\Delta U^s$ , where  $k^s$  is the shear stiffness. With the chemo-mechanical processes any two particles that contact each other become bonded by the cementation that results from neck growth. Thus the contact model changes from the unbounded contact model to a parallel bond model.

The parallel bond model [39] defines the constitutive behavior of a finite-sized piece of cementitious material deposited between two particles. These bonds construct an elastic interaction relationship between particles that works together with the slip models. The parallel bond model simulates the effects of chemical bonding by adding a tension-contact with a defined stiffness and resistance to bending on the axis of the particles but allows slip between them. The elastic force-increments occurring over each mechanical time-step of  $\Delta t_m$  are calculated for particle  $i$  as

$$\begin{cases} \Delta \bar{F}_i^n = (-\bar{k}^n A \Delta U_i) n_i \\ \Delta \bar{F}_i^s = -\bar{k}^s A \Delta U_i^s \end{cases} \quad (12)$$

where  $\bar{k}^n$  and  $\bar{k}^s$  are the stiffness in the normal and shear direction of the material, respectively,  $A$  is the area of the bond cross-section and  $\Delta U_i = V_i \times \Delta t_m$ ,  $V_i$  is the relative velocity of particle  $i$  relative to particle  $j$ . This is an efficient way to use the parallel bond model to represent the mechanical behavior of the granular material following chemical compaction, especially to determine how the stiffness and strength of the material grows as a consequence of chemical creep. The product of stiffness  $k$  and bond area  $A$  can be considered as a new stiffness for each contact. From Eq. (12), it is clear that the contact stiffness will increase with an increase in the contact area  $A$ .

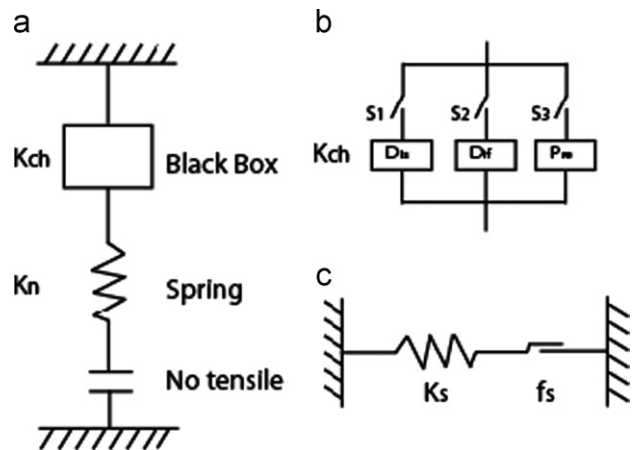


Fig. 3. Contact model for the cycling in PFC<sup>2D</sup> accommodating the constitutive model. New constitutive model shown in (b) is implemented for the force-displacement law.

2.2.2. Constitutive model

A new constitutive model is added to accommodate the behaviors induced by chemical compaction (see Fig. 3, three parallel elements are used to represent the three processes). This includes a spring element with a constant stiffness and a dashpot element where the viscosity is updated in each time step to match the chemical processes [40]. The constitutive equation in the form of the central difference approximation is given as

$$f^{t+1} = \pm 1 / \left( \frac{1}{K} + \frac{\Delta t}{2D} \right) \left\{ u^{t+1} - u^t \mp \left( -\frac{1}{K} + \frac{\Delta t}{2D} \right) f^t \right\} \quad (13)$$

Here,  $f^{t+1}$  and  $f^t$  are the contact normal force at the current and previous time steps,  $K$  is a constant spring stiffness and  $D$  is a variable viscosity of dashpot which is updated in each time step to represent the creep behavior controlled by chemical compaction.  $D$  can be derived simply as

$$D = f / \dot{U}^{ch} \quad (14)$$

where  $f$  is the normal contact force and  $\dot{U}^{ch}$  is the overlap of particles in contact that results from the chemical processes. An

overall cycling within the coupling model calculation starts with mechanical compaction over the short mechanical time step  $\Delta t_m$  to calculate the mechanical force balance and then applies chemical compaction to the system on a different time step  $\Delta t$  until the chemical strains are equilibrated. As noted previously the contact force and velocity is the link between the chemical and mechanical models. The dashpot element is used to satisfy the constitutive requirement induced by the chemical creep behavior. This procedure continues until either the stress at each contact decreases below the critical stress at which pressure solution proceeds or the concentration of the dissolved mineral in the water film of the grain–grain contact and pore space reach equilibrium solubility. This iterative process is implemented within the user-defined model (UDM).

A comparison is completed between this model and that of Revil et al. [29] and shown in Fig. 4. Porosity decreases with time and follows a similar same trend in these two models with the same initial condition. But the model in this paper (the solid line) shows the greater and more rapid loss in porosity with time compared with the model of Ref. [29] (the line with circles). There are several reasons for these differences. The first is that the particle size distribution in each case follows a normal distribution, but the size range is broader in this work, from 0.01  $\mu\text{m}$  to 1000  $\mu\text{m}$ . There are more small particles in the system and smaller particles will dominate the pressure solution compaction rate by increasing the rate [40,41]; also in this work, neck growth induces mass redistribution which will be described in next section and also has an influence on the compaction rate — the process of neck growth increases the contact area, decreases the compaction rate and ultimately exerts a strong influence on the strength of the granular material.

### 2.3. Mass redistribution

A granular aggregate is a system where the mass redistribution is not uniform due to the heterogeneous distribution of the pore space. Chemo–mechanical compaction drives mass redistribution and the system becomes more uniform with stress-mediated dissolution removing porosity. This occurs as the concentration gradient drives diffusion and transports mass to fill pore space by enlarging individual particle sizes and by growing cementitious necks. These in turn allow the combined mechanical and chemical loading to drive compaction and to compact the granular assemblage.

The main effect of mass redistribution is dissolution at each stressed contact. Change in the size of each particle is evaluated as a

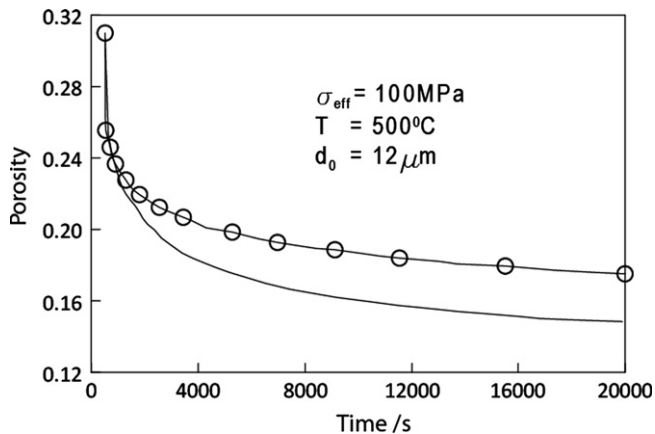


Fig. 4. Comparison of porosity evolution with the model of Revil et al. [29], the line with circle is for the data from Revil et al. [29]; the other solid line is the numerical result of this work.

result of the dissolved mass reprecipitated onto the surface of an individual grain (see Fig. 1(e)). Each target particle  $i$ , is surrounded by several pores and contacts. For each contact, a part of the mineral mass transported into the pore within the fluid reprecipitates on the free surface of pore. For each particle, mass only precipitates on the free surface in contact with the pore. However for the granular mechanics model the individual particles must remain either circular (2D) or spherical (3D). We solve this dichotomy by allowing the particles to grow isotropically by the amount that would deposit on the open pore surface (excluding the contact) and extend this circular contour over the contact (see Fig. 1). This fictitious contact is overclosed within the contact and is accommodated. This allows the particle to grow at the correct rate on the pore wall with a fictitious overlap at the contact that is corrected for this excess interpenetration. This is calculated at the end of each chemical-cycling time-step. For the specific contact between target grain  $i$  and pore  $j$  which is one of pores around  $i$ , the mass reprecipitated onto particle  $i$  is evaluated as

$$\Delta M_i = V_p \frac{A}{M} k_- (C_{pore} - C_{eq}^h) \times \Delta t_{ch} \times \frac{A_i}{A_{ij}} \quad (15)$$

where  $\Delta M_i$  is the mass reprecipitated on particle  $i$ , and  $A_i$  is the area of the pore wall of particle  $i$  and  $A_{ij}$  is the total tributary pore wall area present at the contact of particles  $i$  and  $j$ . Assuming there are  $n$  pores around particle  $i$ , therefore the total mass  $M_i^T$  on the particle is given as

$$M_i^T = \sum_{j=1}^n \Delta M_j \quad (16)$$

and particle  $i$  grows by radius  $\Delta r$  in one time step as

$$\Delta r = \frac{M_i^T}{\rho} \frac{1}{\sum A_i} \quad (17)$$

where  $\rho$  is the density of the material and  $\sum A_i$  is the total free surface of target particle  $i$  in pore space.

For an hydraulically open system with boundary influx, assuming a steady state influx of boundary water,  $Q$ , and revisiting the pore fluid mass balance yields a flowing system form of Eq. (8)

$$\dot{C}_p V_p = \frac{dM_{prec2}}{dt} + D(\tilde{C}_n - \tilde{C}_p) - Q\tilde{C}_p \quad (18)$$

The term of  $Q\tilde{C}_p$  will affect the mass redistribution processes of the system. If it is greater than that mass rate diffusing from the vicinity of the contact periphery then there is no mass reprecipitated on the pore wall of particles. Conversely, when it is smaller than the diffusing mass rate, particles will grow by precipitation since mass diffusion rate is greater than mass efflux with the water flow.

### 3. Strength

We use this model to explore the evolution of permeability and strength in aggregates where chemical–mechanical effects are coupled. This requires that mechanistically consistent rules are applied to determine permeability and strength from the evolution of porosity and the form of bonding at grain–grain contacts. A capillary model is used to represent the form of the fluid transport path around the deforming and interpenetrating particles and the evolution of the cross-sectional area between particles is used to define the evolution of cohesion in the assemblage and therefore its change in strength.

### 3.1. Neck growth and shape change

Chemical processes elevate the mass concentration in the water film at the contact face. Molecular diffusion transports material spontaneously along the periphery of the contact that increases the mass concentration above the hydrostatic solubility. The response to this is the resulting neck growth with mass precipitation assuming the increase in neck size is uniform and formed by mass deposited around the grain contact (see Fig. 2(b,c)).

Neck growth with chemical compaction affects both the chemo-mechanical processes and the evolution of the mechanical properties of the system. Neck growth increases the contact area which is one of the parameters controlling the dissolution rate, as noted in Eq. (2) — the contact stress decreases with an increase in contact area which reduces one principal mechanism driving chemical compaction. The second effect of neck growth is to bond contacting particles — this increases the cohesion and changes the tensile strength from null to some prescribed magnitude (25 MPa for quartz) as representative of the granular system.

### 3.2. Friction and cohesion

Strengthening of each contact is evaluated in terms of the Coulomb failure criterion [38]

$$\tau = C + \mu\sigma_n \quad (19)$$

where  $C$  is the cohesion (that does not depend on normal stress) and  $\mu$  is the coefficient of internal friction. Cohesion reflects the strength of the bonds between particles and the value of cohesion is the combined magnitude of shear strength and normal strength of the bonding between grains. Friction, on the other hand, reflects the strength of particles or asperities that resist slip between sliding particles [42]. Thus, the friction coefficient is approximately the ratio between shear strength and normal strength of asperities. With mechanical and chemical compaction, the friction coefficient will remain constant [43], but the cohesion will change with the bonding of particles changing as a result of cementation and neck growth. So the strength of the granular aggregate may be expected to increase as the size of the bond between particles increases with the process of chemical compaction. We rewrite the Coulomb failure criterion as

$$\tau_{max} = \sigma\mu + S_0A_c/A_{mx} \quad (20)$$

where  $\tau_{max}$  is the shear strength,  $S_0$  is cohesion for quartz which is around 25 MPa;  $A_c$  and  $A_{mx}$  are the cross-sectional area of the contact in the current time step and the possible maximum section area of particle–particle contact area respectively. In this work the Hoek–Brown failure criterion is used to evaluate the global cohesion  $C$  of the granular system during chemical compaction [44,45]. To implement this the contact force is required for each contact to define as set of complementary normal and shear stresses ( $\sigma_n$ ,  $\tau$ ) that act on each grain–grain contact and which can be defined from the contact force applied over each contact area. With linear regression the average friction angle  $\phi$  and coefficient of cohesion  $C$  may be expressed as

$$\phi = \arctan \frac{\eta \sum \sigma_n \tau - (\sum \tau \sum \sigma_n)}{\eta \sum (\sigma_n)^2 - (\sum \sigma_n)^2}$$

$$C = \frac{\sum \tau}{\eta} - \frac{\sum \sigma_n}{\eta} \tan \phi \quad (21)$$

where  $\eta$  is the number of grain–grain contacts that may change during the coupling process of chemical–mechanical compaction.

## 4. Numerical model and results

The model was assembled and executed using the granular mechanics algorithm described previously for each model the initial porosity was set to be about 16% with the particle radius following the Gaussian distribution [46] with the mean and standard deviation defined as

$$\begin{aligned} u &= (r_{hi} + r_{lo})/2 \\ \theta &= (r_{hi} - r_{lo})/2 \end{aligned} \quad (22)$$

where  $u$  is the mean value, and  $\theta$  is the standard deviation of the Gaussian distribution and  $r_{hi}$  and  $r_{lo}$  are the radius of the largest particle and the smallest particle, respectively. To yield a uniform starting porosity of 16% the grain size of the pack is adjusted once it has been assembled (see Fig. 11). The model was executed to estimate the strength evolution during chemical compaction by analysis of the evolving parameters of contact area, cohesion, and stress state. The parameters utilized in the model are listed in Table 1.

### 4.1. Contact area and cohesion

The reduction in porosity during chemo–mechanical compaction has significant influences the strength of the assemblage of particles due to the development of the quality of the contacts [16] (contact number and contact area). It is apparent that as particles merge together by chemical compaction that in turn will increase the mean number of contacts experienced by individual particles — the coordination number will increase. Because of this important macroscopic redistribution of mass, the granular aggregate becomes more uniform and stronger. Also with the microscopic transport of mass, the contact area and particle size changes with chemical compaction. Fig. 5 shows the ratio of actual contact area to possible maximum contact area of particle–particle contact changing with the temporal evolution of chemo–mechanical compaction. Compared with the evolution of the strain during chemical compaction, it is clear that the evolution of contact area ratio follows the same trend with the strain evolution — growth of contact area is fastest at early times when contact radius grows most quickly. This results because the contact stress is much larger than the critical stress at early time and drives dissolution at a high rate — but this reduces as the microscopic stress approaches the equilibrium stress as the contact area grows. Here the model responds to different mechanical loading conditions. The contact ratio shows different final magnitudes at different stresses. These changes are from ~0.3 at 20 MPa to ~0.5 at 30 MPa and finally ~0.8 at 50 MPa. This illustrates that the contact area is not a linear relationship with the mechanical loading and that it is related not only to mechanical loading but also to the particle topology and mass redistribution. Dissolved mineral transported from high concentration contact area to contiguous pore space around contact area and then separate out to form neck. With the concentration

**Table 1**  
Parameters utilized in calculations.

Parameter	Value
Diameter $d$ ( $\mu\text{m}$ )	160–220
Temperature $T$ ( $^{\circ}\text{C}$ )	100
Effective stress $\sigma_{eff}$ (MPa)	20, 30, 5.0
Young's modulus $E$ (GPa)	70
Critical stress $\sigma_c$ (MPa)	77.4
Diffusion path width $\omega$ (nm)	4.0 [9,20]
Diffusion coefficient $D_b$ ( $\text{m}^2 \text{s}^{-1}$ )	$4.27 \times 10^{-10}$
Dissolution rate constant $k^+$ ( $\text{mol m}^{-2} \text{s}^{-1}$ )	$1.54 \times 10^{-10}$ [41]
Solubility of quartz $C_{eq}$ (ppm)	30

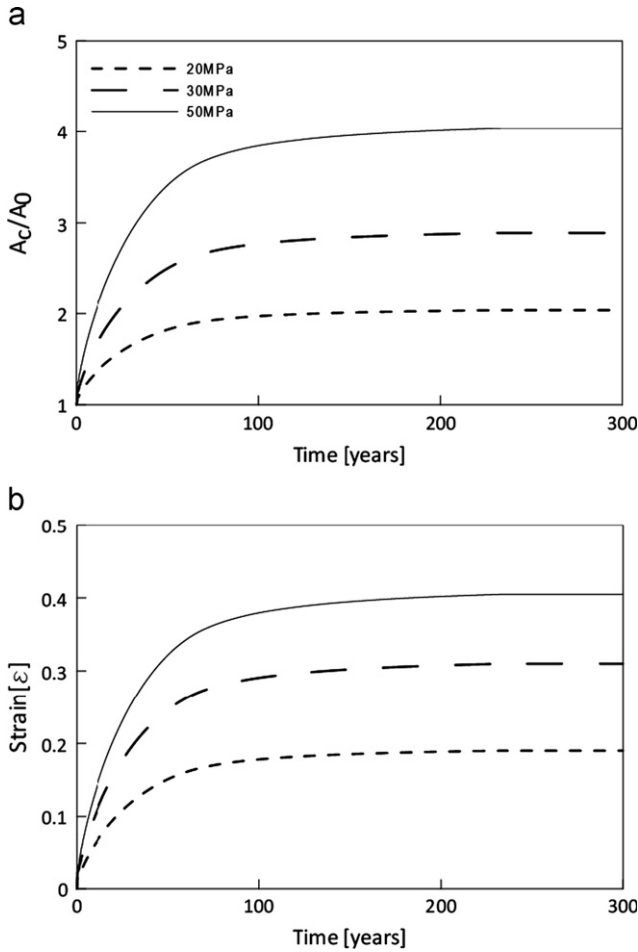


Fig. 5. Growth in contact area ratio (a), defined as the current contact area to the maximum possible contact area of particle–particle contacts with strain evolution (b) for different stresses at  $T=100\text{ }^{\circ}\text{C}$ .

increase of the fluid in the pore, transported mineral will be reprecipitated at the wall to enlarge the ball size, see Fig. 6. The velocity of neck growth is around 10 times faster than that of the particle radius growth, but compared with the evolution of strain, all of them show the same trend which is increasing with the effective stress decreasing and reaches equilibrium state while effective stress equal to critical stress. Also with an increase in the contact area the macroscopic cohesion is expected to increase according to Eq. (20) with the global magnitude of cohesion feasibly evaluated from Eq. (21). The results for this evaluation are shown in Fig. 7. With deformation of the aggregates by chemical compaction the cohesion due to both individual contact area (one particle is  $180\text{ }\mu\text{m}$  and another is  $200\text{ }\mu\text{m}$ ) and for the global system will increase. The cohesion is set to zero at the beginning of the loading before wet, and then set to an intrinsic value which is determined by Hertzian contact induced by purely mechanical loading when wet and then allowed to increase with neck growth by mass redistribution induced by the chemical processes. As a result of this the cohesion increases which will expand the failure envelope (see Fig. 8) even for a constant friction coefficient. Since particles in the model follow a bimodal distribution ( $160\text{--}220\text{ }\mu\text{m}$ ), the small particles dominate the chemical compaction and the cohesion of the global system is a slightly smaller than that in this specific contact.

To evaluate the effective macro scale cohesion of the system we complete numerical compression experiments on a prismatic block with free lateral expansion [47]. The results are shown in

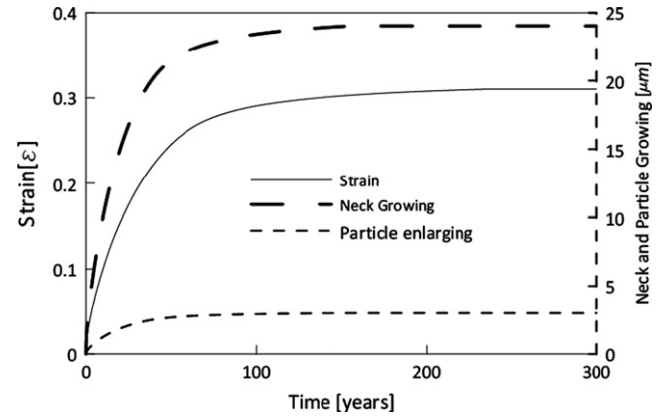


Fig. 6. Evolution of the size of the neck and increment of the radius of a particle in a specific contact with the comparison of the evolution of strain of the granular system during the deformation of the aggregate.

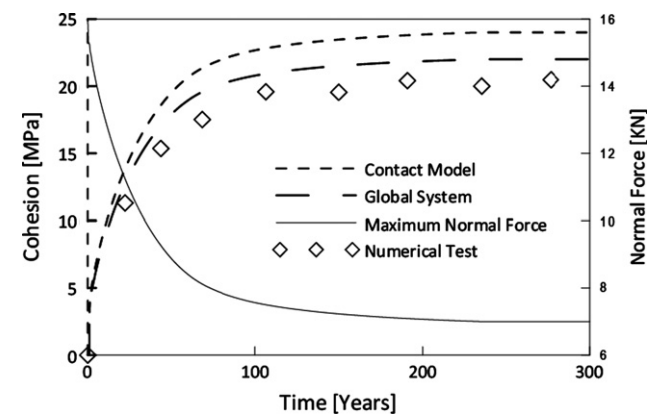


Fig. 7. Evolution of cohesion at an individual contact with particle sizes  $180\text{ }\mu\text{m}$  and  $200\text{ }\mu\text{m}$  compared with global cohesion of the granular system (dashed lines) and cohesion defined for the numerical experiments taken to failure with prior chemo-mechanical compaction.

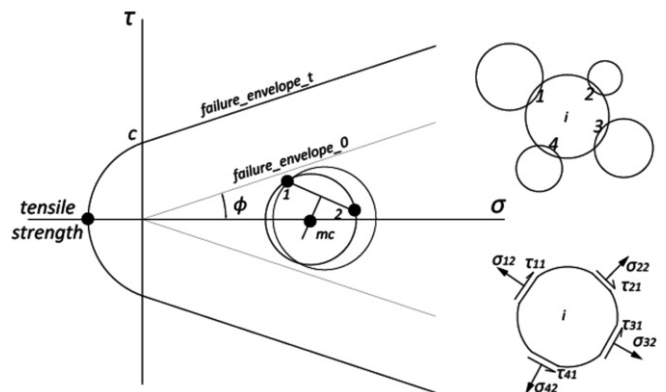


Fig. 8. Change in stress state for a particle with four contacts. Differential stresses drop as the medium concurrently strengthens, driving the stress state progressively further from failure.

Fig. 7. The history of the maximum normal force in the system with the chemical compaction is shown by the solid line which drops from  $\sim 16\text{ kN}$  to  $\sim 7\text{ kN}$ . In this particular instance where the second and third principal stresses  $S_2$  and  $S_3$  are equal to zero. The cohesion is calculated from the principal stress at failure as

$$C = S_1/2 \quad (23)$$

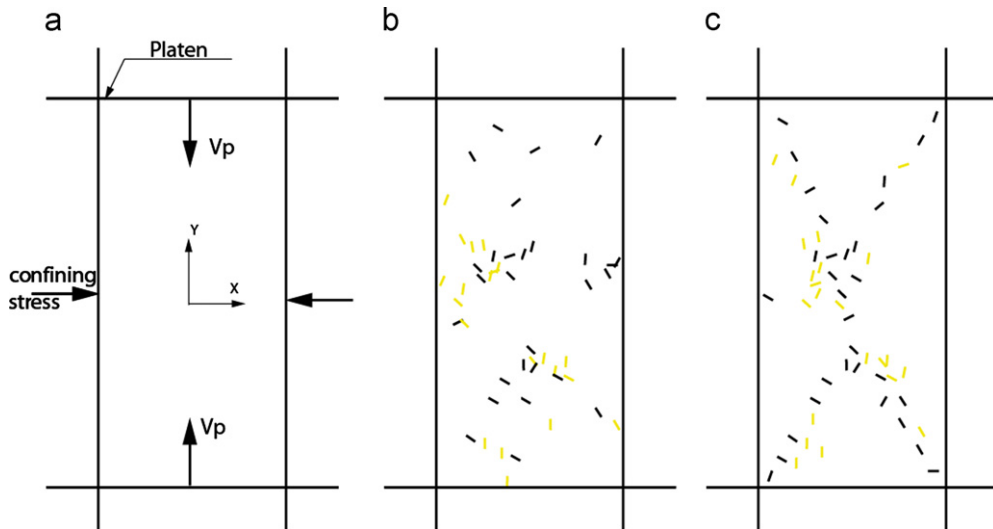


Fig. 9. Comparison of the contact force distribution of the aggregate before and after the chemical compaction. Contact force chain is the driving force for chemical compaction. (For interpretation of the references to color in this figure, the reader is referred to the web version of this article.)

The magnitude of cohesion is close to the estimate recovered from summing the contributions of individual contacts (Eq. (21)), although the difference between the actual and estimated cohesive strengths is not constant because of the inhomogeneity of the system. In all cases the magnitude of the cohesion apparent from the numerical experiments taken to failure is approximately 10% lower than that from the summed strengths of individual contacts.

#### 4.2. Stress state

Another distinct phenomenon in the model is that the contact force diminishes as a result of mass redistribution. The solid line of Fig. 7 shows that the maximum contact force (normal force) decreases with time by a factor of two during chemical compaction (decreases from 16 kN to 7 kN). Fig. 8 shows the stress state of a specific particle  $i$  which has contact with four other particles that surround it. Any two contact stress states of each particle can be represented in the  $\tau$ - $\sigma$  plane. The stress state changes from a large stress differential ( $S_1$ - $S_2$ ) to a smaller differential, which combined with an increase in the strength (cohesion) of the system drives the system progressively further away from the failure envelope.

#### 4.3. Numerical test

To evaluate the strength gain that may occur with chemo-mechanical compaction, we complete a numerical experiment of this laterally constrained system under loading through failure, as illustrated in Fig. 9. The granular model is constrained by the confining stress in the horizontal direction and compacted by constant velocity loading in the vertical direction. Fig. 9(b,c) shows the crack distribution in the model both before and after chemical compaction. The black and yellow short lines indicate locations of rupture driven in either tension or shear, respectively. Cracks are randomly located in the model before chemical compaction due to the effect of the large pores that induce stress concentrations around them. After chemical compaction the cracks are aligned on conjugate failure planes. Fig. 10 shows the stress-strain curve of the numerical experiment and in particular that the strength of the sample after chemical compaction is greater than that before chemical compaction. With almost the same Young's modulus during the initial loading the strength of the

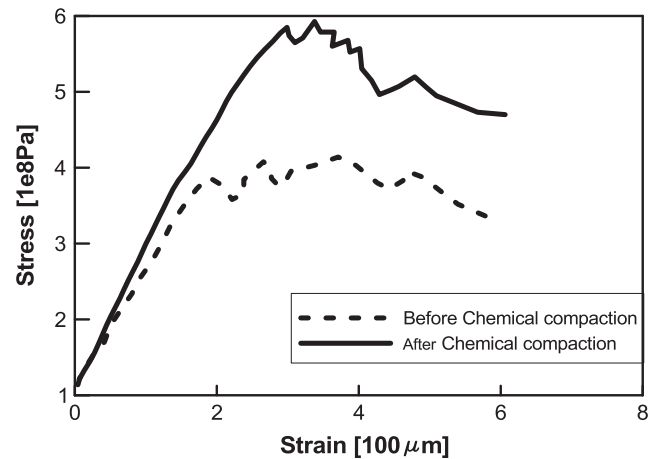


Fig. 10. Model for the numerical experiment (a) and crack distribution in the models before (b) and after chemical compaction (c).

sample after chemical compaction is 580 MPa as compared to only 370 MPa before representing a 54% gain in strength. The reason for this is shown in Figs. 5–8 and 11 in which contact force chain is the driving force for chemical compaction and line thickness denotes the relative magnitude of the contact force. Pore space diminishes with the progress of chemical compaction and contact force becomes more uniform. Because the contact area and coordination number increases, the intrinsic property of cohesion in the system increases, and strength therefore increases. Also, since the porosity also decreases, the force/stress in the sample evolves to a near uniform distribution. Thus, within the system failure nucleates at the weakest point and as the sample becomes more homogeneous these points of nucleation are progressively removed.

### 5. Summary and conclusions

A coupled chemical-mechanical model is used to represent the compaction of a granular system. This is achieved by developing and implementing a new model to represent the granular mechanisms that represent stress-mediated chemical compaction with the three serial processes of dissolution, diffusion and reprecipitation that

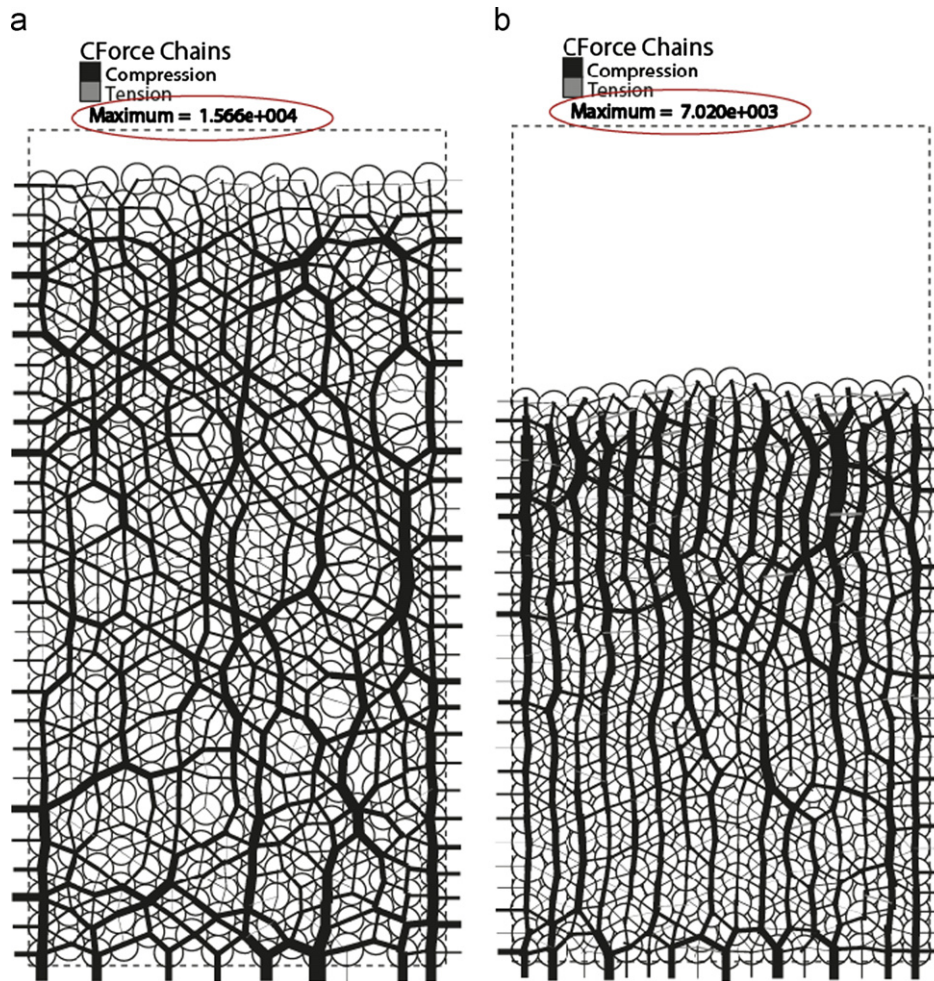


Fig. 11. Stress–strain curves for the laterally constrained numerical experiment both before and after chemical compaction.

redistribute mineral matter. A three element model is successfully used to represent the microscopic mass transport which enlarges the particles by overplating and grows the cementing necks present at each contact. Bead packs with different particle size following Gaussian distribution were used to explore the strength evolution — each with a common porosity of  $\sim 16\%$ .

Chemo–mechanical compaction has a significant influence on transport properties such as porosity and permeability but it also exerts a significant influence on mechanical behavior. Properties such as density of the assemblage of particles and the cohesion of the grain–grain contact increase with the progress of chemical creep due to mass distribution not only at the macroscopic scale as particles interpenetrate and merge into each other but also at the microscopic scale by precipitation on the pore walls and by enlarging particle diameter and growing bonding necks. Monitoring the history of growth of grain–grain contact areas as a proxy for strength increase shows that this area grows with chemical compaction. If cohesion is added as an intrinsic property then the strength of the granular assemblage will also increase. The numerical experiment and summation of particle–particle contacts show close agreement, both indicating an increase in strength with the growth of the neck. Another feedback is that the stress or contact normal force changes with chemical compaction which reduces the influence of stress concentration and correspondingly increases the strength of the granular aggregate. Apparent in the evolution of the system is that creep compaction redistributes the force chains within the system — forces are more homogeneously distributed where creep compaction is allowed to occur. As a result of this the strength of the material is

significantly increased. As the result the numerical experiment, the strength increased after the chemical compaction because of the increase in sectional area and growing of neck of each particle–particle contact to increase the cohesion of the system and the corresponding decrease in the stress concentration. Although dependent on the choice of parameters, this increase in stress was shown to be of the order of 50%.

#### Acknowledgment

This work is the result of partial support from the Department of Energy Office of Energy Efficiency and Renewable Energy and Geothermal Technology Program under contract EE-10EE0002761. This support is gratefully acknowledged.

#### References

- [1] Tadokoro K, Ando M. Evidence for rapid fault healing derived from temporal changes in S wave splitting. *Geophys Res Lett* 2002;29:1047–51.
- [2] Dieterich JH. Time-dependent friction in rocks. *J Geophys Res* 1972;77:3690–7.
- [3] Marone C. Laboratory-derived friction laws and their application to seismic faulting. *Annu Rev Earth Planet Sci* 1998;26:643–96.
- [4] Ruina A. Slip instability and state variable friction laws. *J Geophys Res* 1983;88:359–70.
- [5] Dieterich JH. Modeling of rock friction 1. Experimental results and constitutive equations. *J Geophys Res* 1979;84:2161–8.

- [6] Yasuhara H, Marone C, Elsworth D. Fault zone restrengthening and frictional healing: the role of pressure solution. *J Geophys Res Solid Earth* 2005;110: B06310.
- [7] Yasuhara H. A mechanistic model for compaction of granular aggregates moderated by pressure solution. *J Geophys Res* 2003;108:2530–42.
- [8] Yasuhara H, Elsworth D, Polak A. Evolution of permeability in a natural fracture: significant role of pressure solution. *J Geophys Res Solid Earth* 2004;109: B03204.
- [9] Revil A. Pervasive pressure-solution transfer: a poro-visco-plastic model. *Geophys Res Lett* 1999;26:255–8.
- [10] Bemer E, Lombard JM. From injectivity to integrity studies of CO<sub>2</sub> geological storage chemical alteration effects on carbonates petrophysical and geomechanical properties. *Oil Gas Sci Technol* 2010;65:445–59.
- [11] Andre L, Audigane P, Azaroual M, Menjot A. Numerical modeling of fluid-rock chemical interactions at the supercritical CO<sub>2</sub>-liquid interface during CO<sub>2</sub> injection into a carbonate reservoir, the Dogger aquifer (Paris Basin, France). *Ener Convers Manage* 2007;48:1782–97.
- [12] Polak A, Elsworth D, Liu J, Grader AS. Spontaneous switching of permeability changes in a limestone fracture with net dissolution. *Water Resour Res* 2004;40: W03502.
- [13] Bekri S, Thovert JF, Adler PM. Dissolution of porous media. *Chem Eng Sci* 1995;50:2765–91.
- [14] Bekri S, Thovert JF, Adler PM. Dissolution and deposition in fractures. *Eng Geol* 1997;48:283–308.
- [15] Cussler EL. Dissolution and re-precipitation in porous solids. *AIChE J* 1982;28:500–8.
- [16] Niemeijer A, Marone C, Elsworth D. Frictional strength and strain weakening in simulated fault gouge: competition between geometrical weakening and chemical strengthening. *J Geophys Res Solid Earth* 2010;115: B10207.
- [17] Nygard R, Gutierrez M, Hoeg K, Bjorlykke K. Influence of burial history on microstructure and compaction behaviour of Kimmeridge clay. *Pet Geosci* 2004;10:259–70.
- [18] Chester FM, Chester JS, Kronenberg AK, Hajash A. Subcritical creep compaction of quartz sand at diagenetic conditions: effects of water and grain size. *J Geophys Res Solid Earth* 2007;112: B06203.
- [19] Revil A. Pervasive pressure solution transfer in a quartz sand. *J Geophys Res Solid Earth* 2001;106:8665–86.
- [20] Rutter EH. Kinetics of rock deformation by pressure solution. *Philos Trans R Soc A* 1976;283:203–19.
- [21] Paterson MS. Non-hydrostatic thermodynamics and its geological applications. *Eos Trans Am Geophys Union* 1973;54:355–89.
- [22] Sleep NH, Richardson E, Marone C. Physics of friction and strain rate localization in synthetic fault gouge. *J Geophys Res Solid Earth* 2000;105: 25875–90.
- [23] Tada R, Siever R. Pressure solution during diagenesis. *Annu Rev Earth Planet Sci* 1989;17:89–118.
- [24] Dewers T, Hajash A. Rate laws for water-assisted compaction and stress-induced water-rock interaction in sandstones. *J Geophys Res Solid Earth* 1995;100:13093–112.
- [25] He WW, Hajash A, Sparks D. Creep compaction of quartz aggregates: effects of pore-fluid flow — a combined experimental and theoretical study. *Am J Sci* 2003;303:73–93.
- [26] Lehner FK. A model for intergranular pressure solution in open systems. *Tectonophysics* 1995;245:153–70.
- [27] Renard F, Ortoleva P, Gratier JP. Pressure solution in sandstones: influence of clays and dependence on temperature and stress. *Tectonophysics* 1997;280: 257–66.
- [28] Gundersen E, Renard F, Dysthe DK, Bjorlykke K, Jamtveit B. Coupling between pressure solution creep and diffusive mass transport in porous rocks. *J Geophys Res Solid Earth* 2002;107:2317–35.
- [29] Revil A, Leroy P, Ghorbani A, Florsch N, Niemeijer AR. Compaction of quartz sands by pressure solution using a Cole–Cole distribution of relaxation times. *J Geophys Res Solid Earth* 2006;111: B09205.
- [30] Niemeijer A, Di Toro G, Nielsen S, Di Felice F. Frictional melting of gabbro under extreme experimental conditions of normal stress, acceleration, and sliding velocity. *J Geophys Res Solid Earth* 2011;116: B07404.
- [31] Kato N, Hirasawa T. Effects of strain rate and strength nonuniformity on the slip nucleation process: a numerical experiment. *Tectonophysics* 1996;265: 299–311.
- [32] Taron J, Elsworth D. Coupled mechanical and chemical processes in engineered geothermal reservoirs with dynamic permeability. *Int J Rock Mech Min Sci* 2010;47:1339–48.
- [33] Shimizu I. Kinetics of pressure solution creep in quartz — theoretical considerations. *Tectonophysics* 1995;245:121–34.
- [34] Heidug WK. Intergranular solid–fluid phase transformations under stress: the effect of surface forces. *J Geophys Res* 1995;100:5931–40.
- [35] Raj R. Creep in polycrystalline aggregates by matter transport through a liquid-phase. *J Geophys Res* 1982;87:4731–9.
- [36] Taron J, Elsworth D. Constraints on compaction rate and equilibrium in the pressure solution creep of quartz aggregates and fractures: controls of aqueous concentration. *J Geophys Res Solid Earth* 2010;115: B07211.
- [37] Carslaw HS, Jaeger JC. *Conduction of heat in solids*. 2nd ed. Oxford: Clarendon Press; 1986.
- [38] Goodman RE. *Introduction to rock mechanics*. New York: Wiley; 1980.
- [39] Itasca-Consulting-Group-Inc. *PFC<sup>2D</sup> (Particle Flow Code in 2 Dimensions)*. Minneapolis; 2007.
- [40] Zheng B, Elsworth D. Evolution of permeability in heterogeneous granular aggregates during chemical compaction: granular mechanics models. *J Geophys Res Solid Earth* 2012;117: B03206.
- [41] Niemeijer A, Spiers CJ, Bos B. Compaction creep of quartz sand at 400–600 degrees C: experimental evidence for dissolution-controlled pressure solution. *Earth Planet Sci Lett* 2002;195:261–75.
- [42] Jaeger JC, Cook NGW, Zimmerman RW. *Fundamentals of rock mechanics*. 4th ed. Oxford: Wiley-Blackwell; 2007.
- [43] Muhuri SK, Dewers TA, Scott TE, Reches Z. Interseismic fault strengthening and earthquake-slip instability: friction or cohesion? *Geology* 2003;31: 881–4.
- [44] Hoek E. Estimating Mohr–Coulomb friction and cohesion values from the Hoek–Brown failure criterion. *Int J Rock Mech Min Sci* 1990;27:227–9.
- [45] Hoek E. Reliability of Hoek–Brown estimates of rock mass properties and their impact on design. *Int J Rock Mech Min Sci* 1998;35:63–8.
- [46] Van Bramer SE. A brief introduction to the Gaussian distribution, sample statistics, and the Student's t statistic. *J Chem Educ* 2007;84:1231–2.
- [47] Alexandridis A, Gardner NJ. Mechanical-behavior of fresh concrete. *Cem Concr Res* 1981;11:323–39.